doi:10.1038/nature14417

SUPPLEMENTARY METHODS

MOCVD growth of ML MoS_2 and WS_2 films. As illustrated in Fig. 2a, the synthesis of ML MoS_2 and WS_2 was carried out in a 4.3-inch (inner diameter) hot-wall quartz tube furnace. Molybdenum hexacarbonyl (MHC), tungsten hexacarbonyl (THC), diethyl sulphide (DES), which have high equilibrium vapour pressure near room temperature, are selected as chemical precursors for Mo, W, S, respectively, and introduced to the furnace in gas phase. H_2 and Ar are injected to the chamber using separate lines. All the precursors used in our MOCVD growth are commercially available with well-documented safety protocols (MHC: Sigma Aldrich 577766, THC: Sigma Aldrich 472956, DES: Sigma Aldrich 107247). The safety ratings for these precursors require them to be handled inside of a fume hood. (MHC, THC: NFPA rating for health hazard 4, DES: NFPA rating for health hazard 2). The optimum growth parameters for ML MoS_2 and WS_2 films are as follows. We use a total pressure of 7.5 Torr, growth temperature of 550 ^{o}C and growth time (t_0) of 26 hrs. The flow rate of precursors are 0.01 sccm for MHC or THC, 0.4 sccm for DES, 5 sccm for H_2, and 150 sccm for Ar, which were regulated by individual mass flow controllers (MFCs). The low flow rates were used for MHC, THC and DES for the layer-by-layer growth mode. The long growth time (t_0 ~ 26 hrs), is necessary for full ML growth, because of the low growth rate in this regime. NaCl is loaded in the upstream region of the furnace as a desiccant to dehydrate the growth chamber, which significantly increases the grain size, as discussed in Fig. S6. We use a 4-inch fused silica wafer or a 4-inch Si wafer with 285 nm thick thermal SiO_2 as the main growth substrates. Also the growth is possible on Al_2O_3, HfO_2, and SiN (see Fig. S16).

Optical measurements. *Film patterning:* Photolithography was performed to make the hole-array pattern on the MoS_2 film, where a sacrificial layer of PMMA A4 is coated before the

photoresist. O_2 plasma (400 W, 300 s) was used to remove the unwanted MoS_2 and sacrificial PMMA from the SiO_2 surface. The chips were then placed in acetone for 3 hours to thoroughly remove the photoresist and the PMMA residue.

Optical absorption: The absorption measurements were performed with a Shimadzu UV-Vis-NIR Spectrometer under ambient conditions. All measured samples were grown on a fused silica substrate, and a bare fused silica substrate was used as the reference.

Photoluminescence: The photoluminescence (PL) measurements were performed with a 532 nm excitation laser under ambient conditions. The PL spectra from the sample were collected by an imaging spectrometer with a CCD camera, and the PL images were taken directly using band pass filters with the centre wavelength corresponding to 1.9eV for MoS_2 and 2.0 eV for WS_2.

TEM analysis. *Sample preparation:* The ML MoS_2 film grown on a SiO_2/Si substrate was coated by PMMA A2 or A4, and then the substrate was etched in KOH 1M solution at 90 ^oC. After being rinsed in deionized water three times, the PMMA supported MoS_2 film was transferred to a TEM grid, and the chip was annealed in an ultra-high vacuum (10^{-7} Torr) or atmospheric pressure with Ar (100 sccm) and H_2 (100 sccm) flow at 350 ^oC for 3 hours in order to remove the PMMA[19]

DF-TEM: DF-TEM images, along with electron diffraction patterns, were taken using an FEI Tecnai T12 Spirit, operated at 80 keV. The acquisition time for each dark field image was 10 seconds.

ADF-STEM: ADF-STEM images were taken using a Nion Ultra STEM 100 operated at 60 keV. The convergence angle was 30 mrad, and the probe current was about 50 pA.

Device fabrication. For the FET fabrication, we start with an as-grown ML TMD film on 285 nm SiO_2/Si and first define the source and drain electrodes using the standard photolithography

process, followed by e-beam evaporation of 0.5 nm Ti/75 nm Au. After lifting off using Microposit Remover 1165, we then define and etch the conducting channel for FET devices using photolithography and O_2 plasma etching. For top gate fabrication, 30 nm HfO_2 is deposited using atomic layer deposition (ALD) as the dielectric material, followed by the same electrode fabrication process for top-gate electrode fabrication (for top gate WS_2 FETs, we deposit 1 nm Al_2O_3 as the seeding layer for HfO_2 ALD). We also deposit 30 nm HfO_2 on top of the back gated devices. This increases the carrier doping level and the conductance of our devices, enabling reproducible measurements under ambient conditions (see Fig. S17). All devices shown in Fig. 3 and 4 were fabricated using standard photolithography techniques, except for the additional voltage probes (the five thin electrodes in Fig. 3a, inset) which were added later using e-beam lithography. The dimensions (W, width and L, length) of conducting channels are as follows: W 15 μm (Fig. 3a-3c), W 9 μm, L 19 μm (Fig. 3d and 3g), W 7.7 μm, L 3.3 μm (Fig. 3e), W 7.7 μm, L 5.3 μm (Fig. 3f), W 15 μm, L 15 μm (Fig. 4d and 4e). For the fabrication of the multi-stacked device in Fig. 4, the SiO_2 consists of three successive depositions: 100 nm SiO_2 was deposited using PECVD at 30 W and 200 ^oC, followed by 350 nm SiO_2 deposited using PECVD at 140 W and 350 ^oC, and 50 nm SiO_2 deposited using ALD at 200 ^oC.

Electrical measurements. All the electrical measurements (except for Fig. 3c) were done under ambient conditions using a custom-built probe station with an Agilent B1500 Device Analyzer. Both four-probe and two-probe measurements were used to accurately measure the sheet conductance. Comparing the results of four-probe and two-probe measurements, the contact resistivity is estimated to be approximately 50 Ω·mm. For temperature dependent measurements (Fig. 3c), FET devices were wirebonded and measured in a cryostat in vacuum for temperatures down to 77K.

SUPPLEMENTARY NOTES

A. Growth mechanism of layer-by-layer (LBL) growth

We have conducted two experiments to support LBL growth mechanism. First, Fig. S3 presents optical reflection (OR), PL and SEM images taken from our MOCVD grown ML MoS_2 films (average grain size ~ 3 μm) after different growth times (0.8 t_0, 1.0 t_0, and 1.5 t_0). It confirms that additional nucleation on the existing first layer does not occur until the first layer growth is completed and the growth proceeds by enlarging the already-nucleated grains for $t < t_0$, most likely by edge attachment growth. After t_0 (full first layer growth), the nucleation for the second layer occurs at the grain boundaries (GBs) and in the basal plane. The PL intensity images show striking behaviours especially at the GBs. They show much brighter PL uniformly along GBs at $t = t_0$ and much darker PL there when $t > t_0$. The brighter PL at $t = t_0$ is consistent with the PL behaviours previously seen from the tilt GBs in CVD grown MoS_2[19]. This suggests that upon the completion of the first layer growth ($t = t_0$), neighbouring grains are uniformly connected laterally by tilt GBs *before* further growth occurs for the second layer. Once the second layer starts growing on top of the first layer, the PL signal decreases especially along GBs, as the band structure of MoS_2 shifts from direct bandgap (ML) to indirect bandgap (for multilayers). Altogether, our data in Fig. S3 confirm the LBL growth mode in our MOCVD growth and the high-quality uniform intergrain connection at the optimum growth time (t_0). We also note that monitoring PL enhancement along GBs can be used in the future to find the optimum growth time t_0 and to confirm the high quality intergrain connection in the grown film.

The edge attachment growth mechanism for our MOCVD growth is further supported by Fig. S4. Here, we performed a partial growth of ML MoS_2 (step I; $t < t_0$) and re-growth (step II),

where the step II was conducted on the same sample generated after step I. The same film was characterized by optical reflection, PL, DF-TEM after each growth step to observe the location and morphologies of the growth. Our data confirm that during the re-growth, MoS_2 grains continue to grow by edge attachment without generating additional nucleation sites on available SiO_2 surfaces. This is confirmed by the same average number of nuclei (or grains in the first layer) per unit area after step I and step II (0.27 $\mu m^{-2} \rightarrow$ 0.26 μm^{-2}), again indicating that the empty space after step I was completely filled by continued growth of existing grains (along their edges) with the same crystal orientation without creating additional grains.

B. Thermal decomposition of precursors

We studied thermal reaction for DES and MHC using a residual gas analyser (RGA), which connected to the outlet of the furnace and detects the mass signal of the gas residue. Fig. S5 shows the relative intensity ratio for corresponding molecules extracted from mass spectra of RGA. First, we flowed vaporized MHC into the chamber at room temperature (blue circle), and we confirmed that vaporized MHC contains several carbonyl molybdenum, $Mo(CO)_x$. Above 250 ^oC the signal for $Mo(CO)_x$ disappeared, indicating that $Mo(CO)_x$ was completely decomposed. In the case of DES, the intensity profiles at room temperature (blue circle) are almost the same as at growth temperature, 550 ^oC (red circle), with both showing various hydrocarbon sulphides (C_xH_yS) under RGA resolution. This means that the concentration of DES in the furnace barely changed due to its decomposition. According to the RGA study, we summarize the status of precursors at growth temperature: i) the concentration of C_xH_yS is uniform inside the furnace at the laminar flow condition. ii) MHC is decomposed to Mo and delivered by high flow Ar.

C. Dependence of grain size on concentration of H_2, H_2O, and DES

We have already shown the H_2 concentration dependence of grain size in Fig. 2d. The dependence on H_2O concentration was observed under the presence of salt desiccant (NaCl, KCl, NaBr), as shown in Fig. S6a, where the grain size increased up to 100-fold, according to the presence/absence of salt. Also, Fig. S6b shows that the concentration of DES affects the grain size.

In order to explain these phenomena, we need to discuss the precursor decomposition and nucleation kinetics. First, according to hydrolysis and hydrogenolysis[28], H_2 and H_2O promote the decomposition of DES precursor, which enhances the concentration of sulphur vapour. Also, the concentration of sulphur vapour linearly depends on the concentration of DES, since DES contains certain ratio of sulphur vapour. Second, the concentration of sulphur affects the nucleation kinetics and grain size. The assumptions we make are: (i) our growth is Mo diffusion limited growth, since the Mo concentration is kept low for layer-by-layer growth. In comparison, the concentration of DES is much higher than that of Mo vapour. (ii) when a Mo atom produced by thermal decomposition of MHC, arrives at the surface, it diffuses until reacting with sulphur produced by decomposition of DES. (iii) energetically, Mo and S atoms prefer to be adsorbed at a MoS_2 edge. (iv) if the decomposition rate of DES is fast, Mo atoms lose their chance to find energetically favourable positions and nucleation occurs at a non-edge region. Based on these assumptions, we conclude that the nucleation density of MoS_2 increases on the surface when the decomposition kinetics of DES becomes faster. Therefore, when H_2, H_2O, and DES concentrations are high, nucleation density increases and grain size decreases.

SUPPLEMENTARY FIGURES

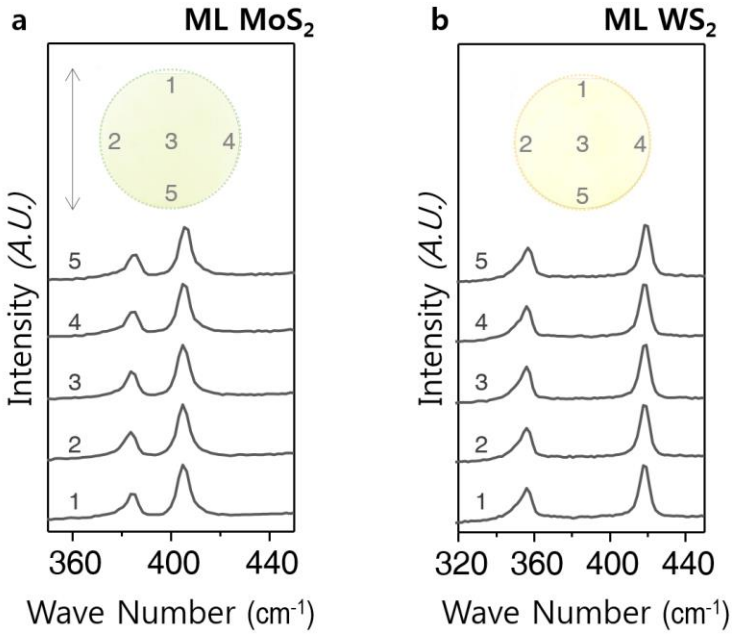

Fig. S1 | Raman spectra for MoS_2 **(a)** and WS_2 **(b)** respectively, taken at different locations marked on the corresponding fused silica wafer.

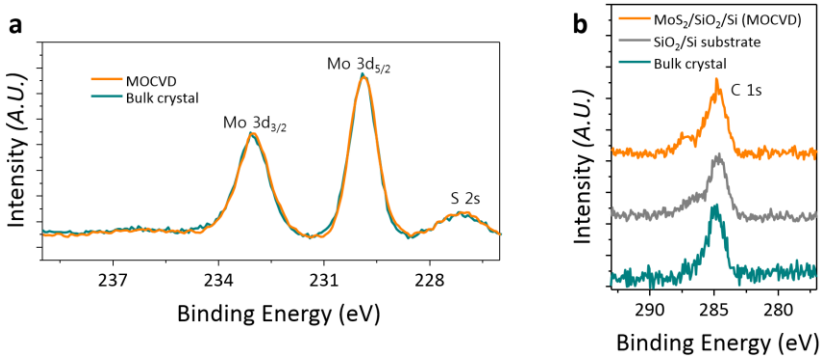

Fig. S2 | XPS spectra of **a,** Mo 3d 3/2, 5/2 and S 2s state for MoS_2 grown by our method (orange) and bulk MoS_2 single crystal (cyan blue), where the peak position and FWHM are almost identical. **b,** C 1s for MoS_2 grown by our method (orange), bare SiO_2/Si substrate after solvent cleaning (grey) and bulk single crystal (cyan blue), where all three sample show similar peak area of C 1s, which means our films do not contain significant carbon residue after MOCVD process (curves shifted from the bottom for clarity).

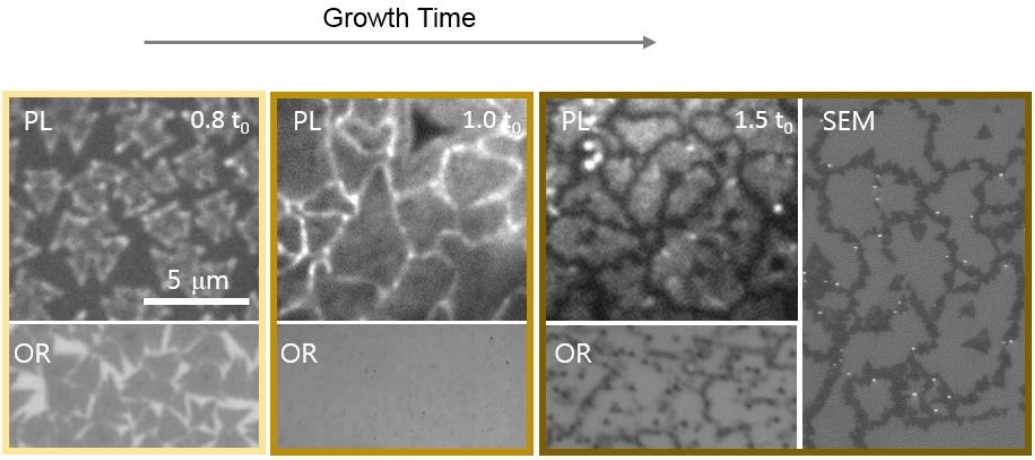

Fig. S3 | Optical reflection, PL, SEM images of MOCVD-grown MoS_2 at different growth times, where t_0 is the optimal growth time for full ML coverage.

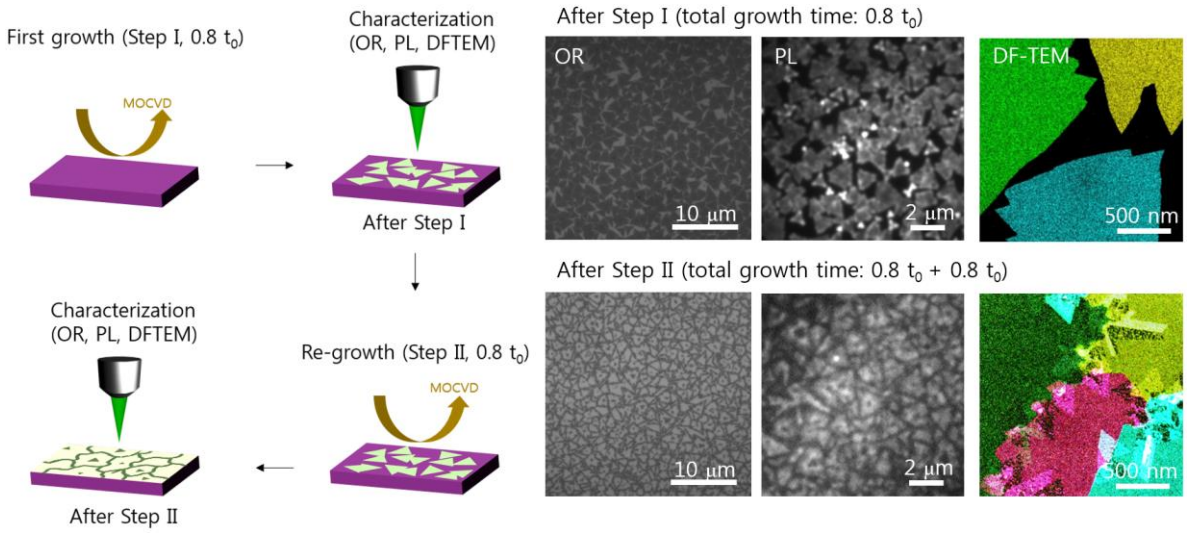

Fig. S4 | Schematics of growth (step I) and re-growth (step II) of MoS_2 film and corresponding optical reflection, PL, DF-TEM images.

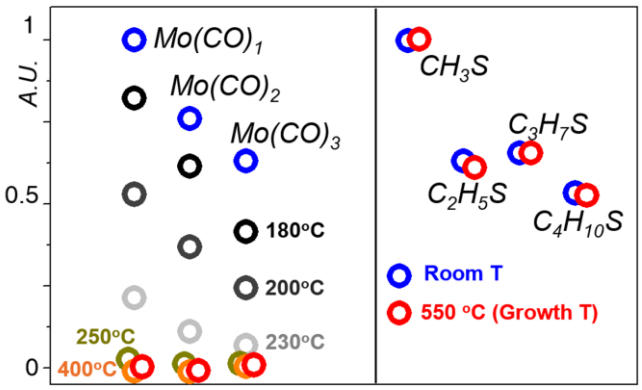

Fig. S5 | Normalized intensity of residual gas signal for $Mo(CO)_x$ and C_xH_yS depending on temperature. Each dot corresponds to a temperature, as denoted in the figure.

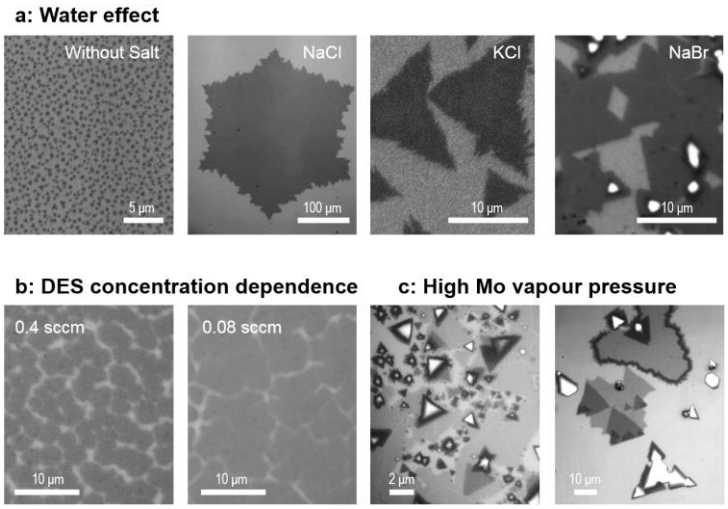

Fig. S6 | Morphology change of MOCVD-grown MoS_2 depending on the growth parameters. In order to show grain size clearly, we intentionally grow partially covered MoS_2. **a,** salt (desiccant) dependence of grain size. **b,** DES flow rate dependence of grain size. **c,** high Mo vapour concentration environment, where a mixture of monolayer, multilayer and no-growth regions exist.

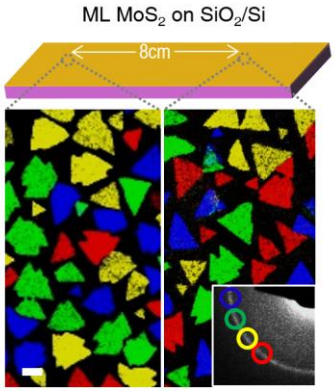

Fig. S7 | False-colour DF-TEM image of MoS_2 grown at two locations 8 cm apart, where the identical grain size and nucleation density suggests the homogeneous nucleation over the whole growth area. Scale bar, 100 nm.

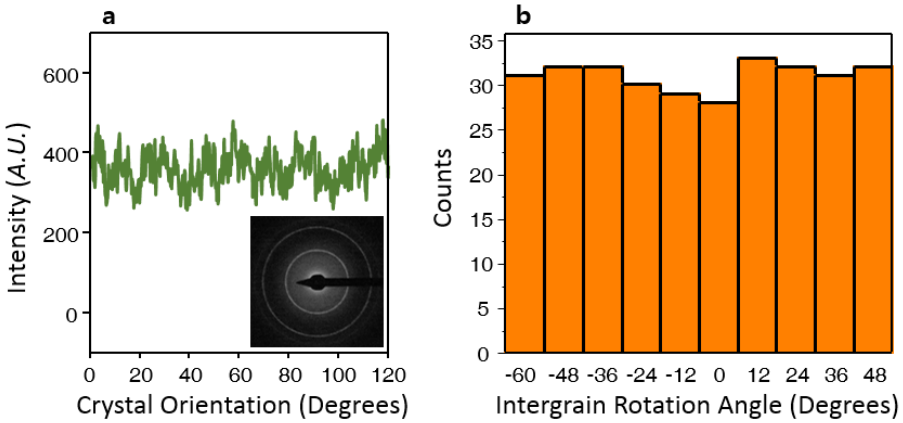

Fig. S8 | **a,** A polar plot of the electron diffraction intensity (diffraction map shown in the inset) measured from a large area ML MoS_2 (inset), indicating a uniform angular distribution of the MoS_2 crystal orientation[32]. It is generated by averaging the diffraction intensity from the three equivalent angular domains, each spanning 120 degrees. **b,** A histogram of intergrain rotation angles measured from all grain boundaries found in the ML MoS_2 sample shown in **Figure 2e**, suggesting no preferred intergrain tilt angle. For this, the crystal orientation for every MoS_2 grain was first obtained from five DF-TEM images taken with different objective aperture locations (each centred at 0º, 12º, 24º, 36º and 48º, respectively)[32]. In each DF-TEM image taken at an objective aperture location θ, we assign the crystal orientation of θ (for brighter regions; from aligned Mo sub-lattice) or θ - 60º (for less bright regions; from aligned S sub-lattice)[19]. The intergrain rotation angles were extracted using these assignments and range between -60º to 60º (with ± 6º error).

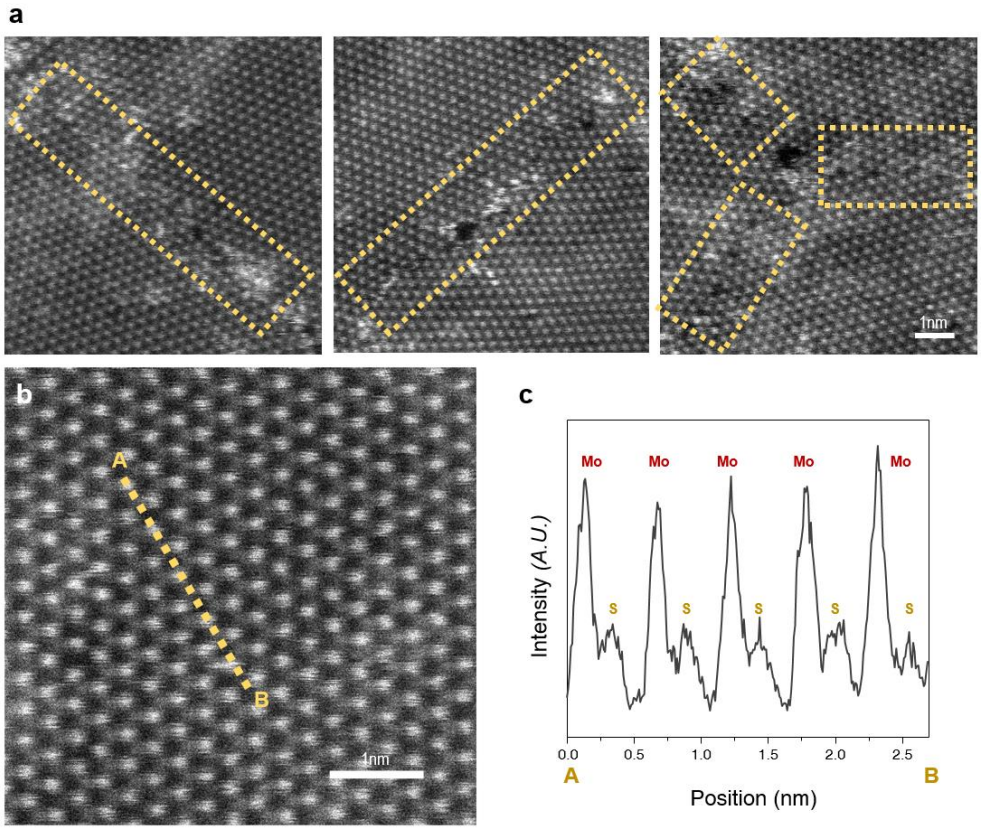

Fig. S9 | **a,** ADF-STEM images of laterally-stitched grain boundaries in a ML MoS_2 film. The sub nanometre holes come from electron beam radiation damage, and the clouds are surface contaminations generated during the transfer process. **b,** High quality ADF-STEM image of ML MoS_2 film and **c,** corresponding line profile of intensity. The image intensity is roughly proportional to Z^{γ}, where Z is the atomic number, and $1.3 < \gamma < 2$.

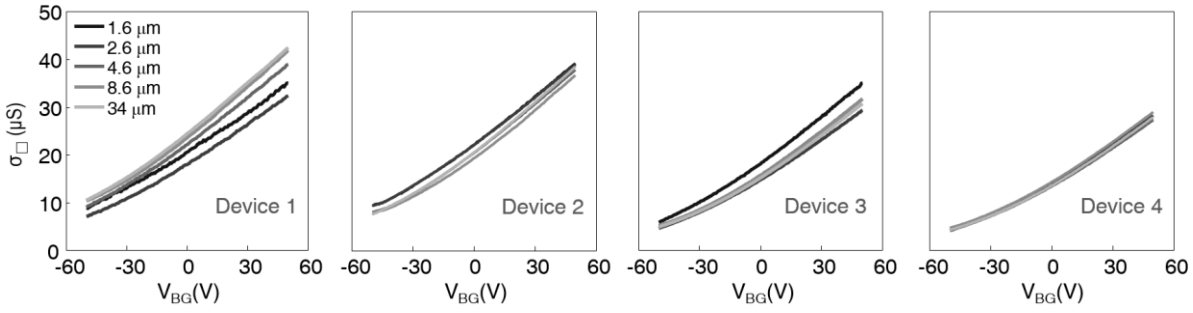

Fig. S10 | Gate-dependent $\sigma_{\square}$ of four multiple-electrode ML MoS_2 FETs (same geometry as shown in Fig. 3a inset) separated by up to 3.3 mm.

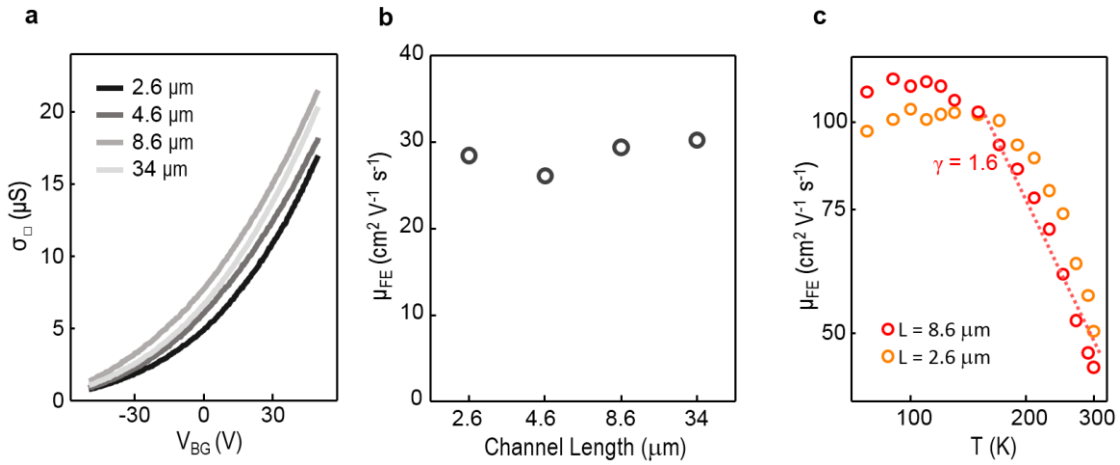

Fig. S11 | **a**, Transfer curves measured from MoS_2 of grain size 3 μm with different channel lengths. **b**, Field effect mobility (μ_{FE}) of different channel lengths extracted from (a). **c**, Temperature dependence of μ_{FE} measured from MoS_2 film of grain size 3 μm, with different channel lengths, which show the same dependence as shown in Fig. 3c.

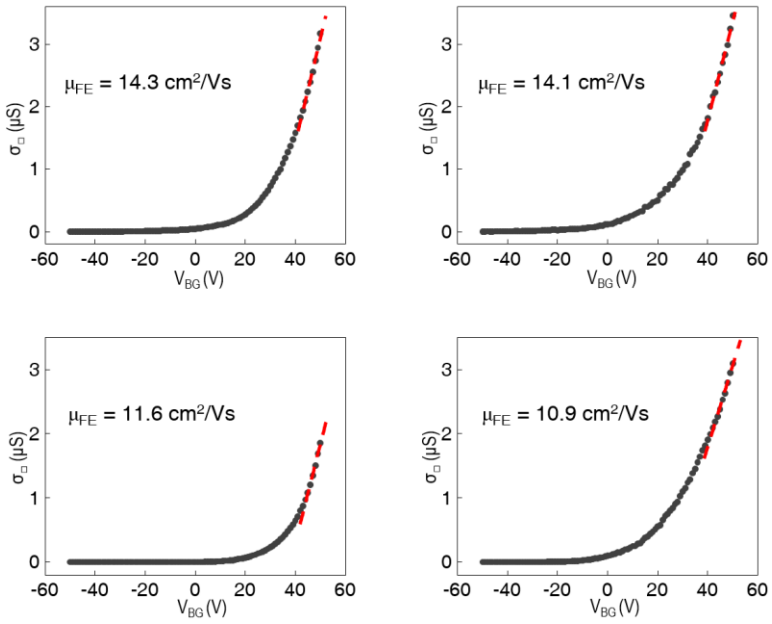

Fig. S12 | Gate-dependent two-terminal $\sigma_{\square}$ of four additional ML WS_2 FETs, of which the extracted mobilities are 14.3, 14.1, 11.6 and 10.9 cm^2/Vs, respectively.

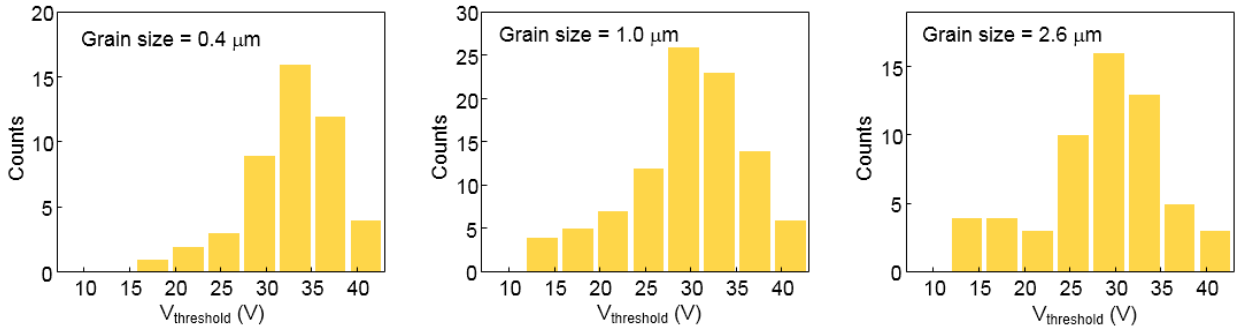

Fig. S13 | Histograms of threshold voltage of MoS_2 FETs with grain size 0.4, 1.0 and 2.6 μm, respectively.

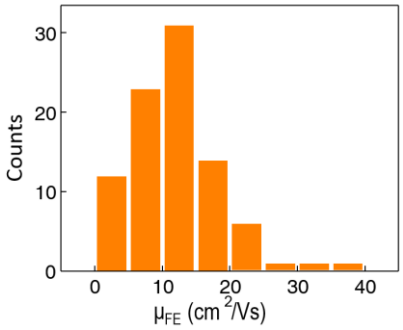

Fig. S14 | Statistics for field effect mobility of MoS_2 FETs taken from the devices in Fig. 3g.

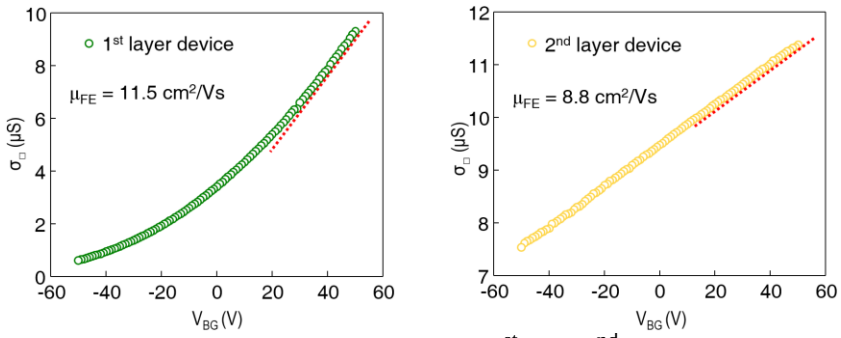

Fig. S15 | Gate-dependent $\sigma_{\square}$ for ML MoS_2 FET on 1st and 2nd layer in the multi-stacked device structure. The total gate oxide (SiO_2) thickness for 1st and 2nd layer devices are 285 nm and 785 nm, respectively.

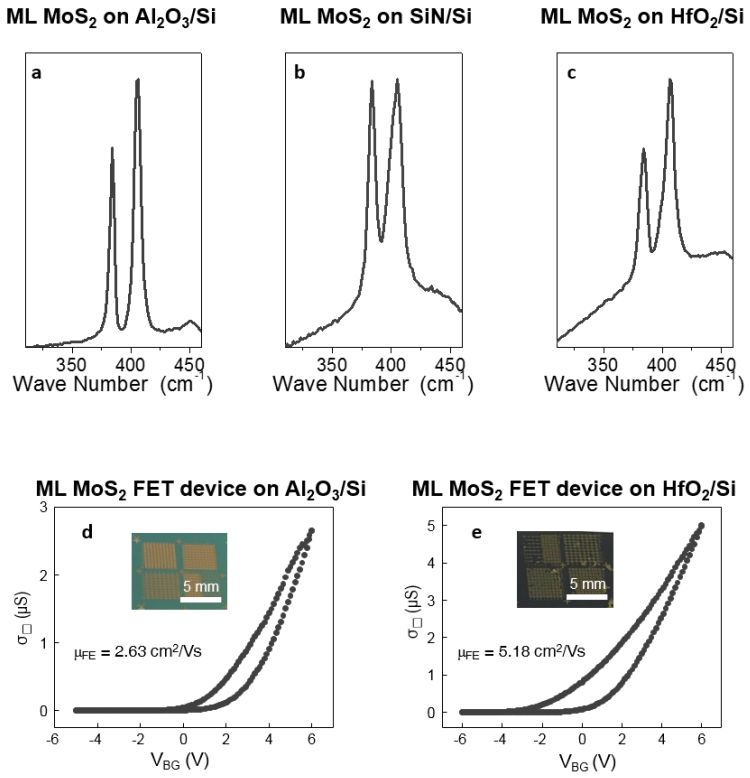

Fig. S16 | **a-c,** Raman spectra for MoS_2 grown on Al_2O_3, SiN and HfO_2 covered Si, respectively. **d-e,** $\sigma_{\square}$-V_{BG} curves for ML MoS_2 FET on Al_2O_3/Si and HfO_2/Si, respectively. The measured dielectric constant for Al_2O_3 and HfO_2 is 6.0 and 15.5, respectively. These MoS_2 films were grown under the same conditions developed for SiO_2 substrates as described in Methods, without any further optimization.

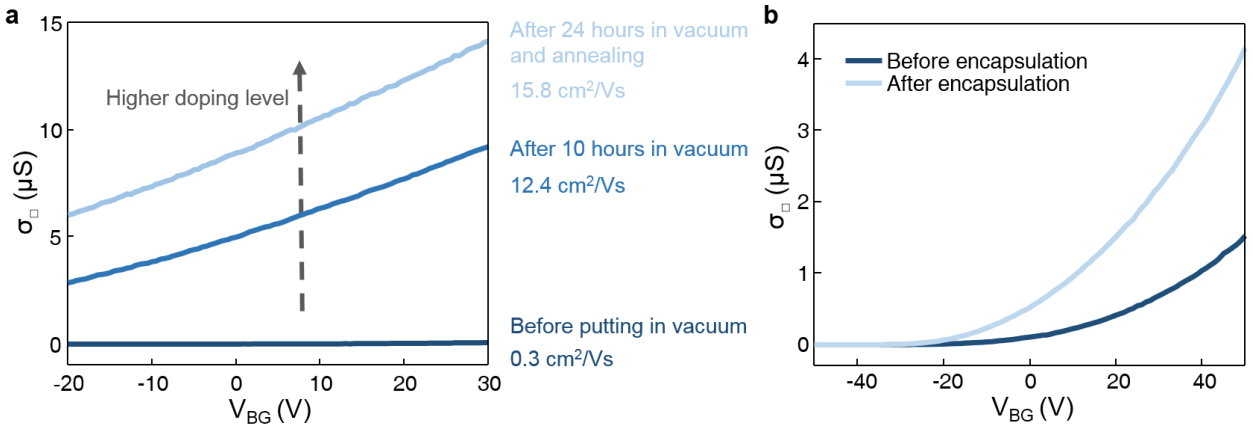

Fig. S17 | **a**, The effect of measuring in vacuum and annealing on the device's electrical performance (the vacuum and annealing n-dope the MoS_2 devices). **b**, The transfer property of same device in ambient before and after HfO_2 encapsulation (encapsulation n-dopes MoS_2).

REFERENCES

31. Havener, R. W. *et al.* High-throughput graphene imaging on arbitrary substrates with widefield Raman spectroscopy. *ACS Nano* **6,** 373–80 (2012).

32. Huang, P. Y. et al. Grains and grain boundaries in single-layer graphene atomic patchwork quilts. *Nature* **469**, 389–392 (2011).